Hydrogen-bonded structure and mechanical chiral response of a silver nanoparticle superlattice

Bokwon Yoon[1], W. D. Luedtke[1], Robert N. Barnett[1], Jianping Gao[1], Anil Desireddy[2], Brian E. Conn[2], Terry Bigioni[2] and Uzi Landman[1]*

Self-assembled nanoparticle superlattices—materials made of inorganic cores capped by organic ligands, of varied structures, and held together by diverse binding motifs— exhibit size-dependent properties as well as tunable collective behaviour arising from couplings between their nanoscale constituents[1-15]. Here, we report the single-crystal X-ray structure of a superlattice made in the high-yield synthesis[16] of $Na_4Ag_{44}(p\text{-MBA})_{30}$ nanoparticles, and find with large-scale quantum-mechanical simulations that its atomically precise structure and cohesion derive from hydrogen bonds between bundled[4] p-MBA ligands. We also find that the superlattice's mechanical response to hydrostatic compression is characterized by a molecular-solid-like bulk modulus $B_0 = 16.7$ GPa, exhibiting anomalous pressure softening and a compression-induced transition to a soft-solid phase. Such a transition involves ligand flexure, which causes gear-like correlated chiral rotation of the nanoparticles. The interplay of compositional diversity, spatial packing efficiency, hydrogen-bond connectivity, and cooperative response in this system exemplifies the melding of the seemingly contrasting paradigms of emergent behaviour 'small is different'[9] and 'more is different'[17].

The $Na_4Ag_{44}(p\text{-MBA})_{30}$ nanoparticles (NPs) have been synthesized in semi-aqueous solution with an all-aromatic p-mercaptobenzoic acid (p-MBA) protective ligand shell[16]. With judicious choice of solvent conditions and stabilizing agents, these fragile and unstable Ag complexes were transformed into chemically inert materials with exceptional stability. The NPs were crystallized from dimethylformamide (DMF) solution, with rhombus-shaped crystals forming after 1–3 days. As the superlattices were grown from DMF solutions, the carboxylates of the ligands must be protonated for the NPs to be soluble in the DMF; consequently, all of the carboxylates were protonated in the crystallized superlattice. The entire structure of the individual NP was determined by single-crystal X-ray crystallography (see Supplementary Information in ref. 16 and inset (i) in Fig. 1), and its stability has been attributed to a closed-shell 18-electron configuration manifested by the opening of a large gap between the occupied and unoccupied energy levels of the superatom electronic spectrum[16].

The X-ray-determined structure of the NP superlattice (NPSL) shown in Fig. 1 and its theoretical analysis reveal intricate bonding characteristics and spatial organization of the NPs. The triclinic unit cell of the superlattice (see unit-cell vectors **a**, **b** and **c** in Fig. 1a,c) contains two silver NPs, denoted as α, β, which are related by a

mirror reflection symmetry, and occupy neighbouring crystalline layers (for different views of the superlattice, see Fig. 1a–d). The layers are stacked as in a face-centred-cubic (fcc) lattice, and because of the above-noted (α ↔ β) mirror symmetry, the layers' stacking periodicity consists of a 6-layer sequence [Aα, Bβ, Cα, Aβ, Bα, Cβ] (Fig. 1a,b); a view in the plane defined by the **a** and **b** vectors (the xy plane), illustrating ABC fcc layer stacking, is shown in Fig. 1c.

Neighbouring NPs interact through a full hydrogen (H)-bond network, formed between the carboxyl (-COOH) groups of interfacing ligands that are thiol-bonded to neighbouring NPs (see Fig. 1d and inset (ii)). The p-MBA ligands bundle in two ways: double-bundles (L_2) and triple-bundles (L_3) (see Fig. 1d, Fig. 3a in ref. 16 and Supplementary Information 1); ligand bundling has been predicted in early investigations of thiol-passivated gold nanoparticles[4]. Intralayer bonding between neighbouring NPs (α–α or β–β) involves interfacing doubly bundled ligands (L_2) NPs, whereas inter-NP interaction between neighbouring α–β NPs located in neighbouring layers involves interfacing triply bundled ligands (L_3); see the inter-NP region along **a** and **c**, respectively, in Fig. 1d. The high connectivity in this molecular-framework superlattice (where about half of the volume is void, see X-ray summary in the Supplementary Information to ref. 16) involves interactions between 30 interfacing pairs of p-MBA ligands from a $Na_4Ag_{44}(p\text{-MBA})_{30}$ NP and its nearest neighbours in the superlattice, making 60 H bonds (24 intralayer and 36 interlayer) between an NP and its neighbours. The average hydrogen-bond length (defined as the distance between the H atom and the acceptor oxygen atom, O_a) is $d(H–O_a) = 1.536$ Å ± 0.019 Å, the distance between the acceptor and donor oxygen atoms is $d(O_d–O_a) = 2.574$ Å ± 0.015 Å, and the angle $\angle (O_dHO_a) = 177.418° \pm 0.719°$. Formation of the superlattice has little effect on the structural parameters of the metal cores of the silver NPs (Supplementary Information 1).

The cohesive energy of the NPSL, obtained from calculations (Methods) of the difference between the total energy of two isolated silver NPs taken in the configuration found in the superlattice, and the total energy of the superlattice made by a periodic replication of the two-NP triclinic unit cell, is 24.0 eV. This can be expressed as $E_{coh} = 24.0$ eV/(30 ligand pairs) $= 0.80$ eV assigned to a pair of hydrogen-bonded p-MBA ligands (each anchored to one of the neighbouring interacting NPs), that is, 0.40 eV per H bond. For comparison, we remark that the calculated binding energy between an isolated pair of hydrogen-bonded Ag(p-MBA) molecules is 0.847 eV (0.423 eV per H bond), indicating that the binding between the NPs in the superlattice is dominated by the H bonds between

[1]School of Physics, Georgia Institute of Technology, Atlanta, Georgia 30332-0430, USA, [2]Department of Chemistry and School of Solar and Advanced Renewable Energy, University of Toledo, Toledo, Ohio 43606, USA. *e-mail: Uzi.Landman@physics.gatech.edu
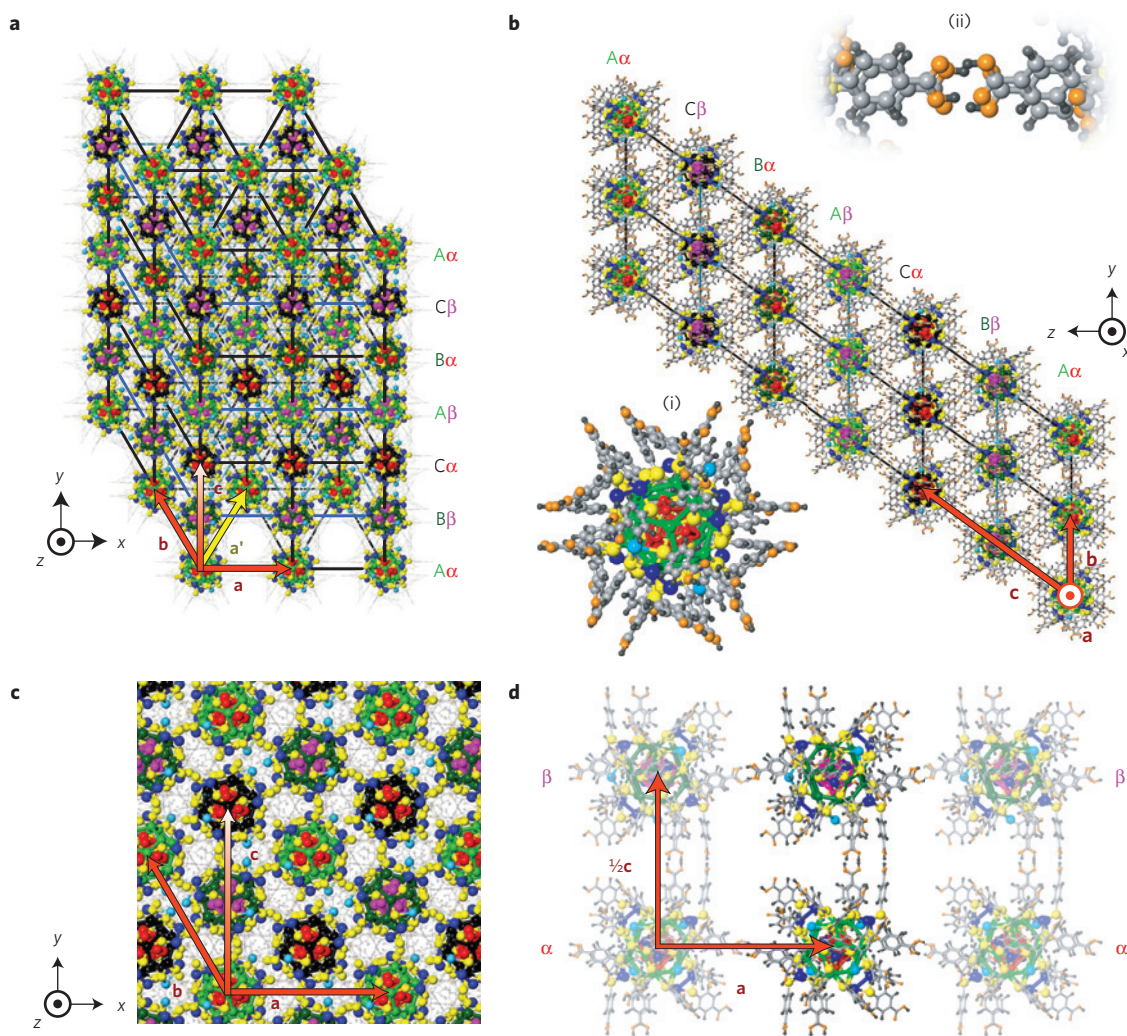
1

Figure 1 | Ag$_{44}$(*p*-MBA)$_{30}$.Na$_4$ superlattice structure. a–d, A three-dimensional view of the superlattice structure with the triclinic unit-cell vectors denoted at the bottom left; **a** = **b** = 26.018 Å, **c** = 51.551 Å (V_0 = 24558.456 Å^3), and ∠ (**a**,**b**) = 120°, ∠ (**b**,**c**) = 59.688° and ∠ (**a**,**c**) = 90°. An alternative unit cell, close to a rhombohedral shape, is given by the vectors **a′**,**b**,**c** (see **a′** coloured yellow) with the same lengths as before but with ∠ (**a′**,**b**) = 60°, ∠ (**b**,**c**) = 59.688° and ∠ (**a′**,**c**) = 59.688°. The unit cell contains two silver NPs, one at the origin (inner core Ag$_{12}$ atoms coloured red) and the other (inner core Ag$_{12}$ atoms coloured pink) located at **c**/2. A view of a single NP is given in inset (i), with a Ag$_{12}$ empty icosahedral inner core (red), a surrounding Ag$_{20}$ dodecahedral shell coloured green, and twelve outer silver atoms (coloured dark blue) distributed among the six Ag$_2$S$_5$ mounts. The S atoms are coloured yellow, and C, O and H (smallest spheres on the NP's outer shell) atoms are coloured grey, orange and light blue, respectively. The silver NPs are organized in layers (defined by the **a** and **b** vectors) with each of the layers consisting of identical NPs (see **b** for a view of the plane defined by the vectors **b** and **c**, and **c** for a view of the (**a**,**b**) plane). On the other hand, the NPs in neighbouring layers (denoted as α and β NPs, see **a**–**d**) are related by a mirror reflection in the x = 0 plane (that is, (x, y, z) → (−x, y, z)) followed by a translation by **c**/2. The layers are stacked as in a fcc lattice (with the 3-layer stacking sequence denoted as A, B, C). The NPs in each layer form a (filled) hexagonal lattice (see **c**). The fcc ABC stacking is evident in **a**–**c**, with the A, B and C layers distinguished by colouring the Ag$_{20}$ dodecahedron light green (A), darker green (B) and black (C). The stacking of the layers is depicted clearly in the xy 3-layer projection shown in **c**, where the A layer is defined by the **a** and **b** vectors, the B layer is the one located at **c**/2, and the C layer is given by the tip of the **c** lattice vector. The tip of the arrow corresponding to the vector **c** is shown in a lighter shade to indicate that it is out-of-the **ab** (or xy) plane orientation. As illustrated in the three-dimensional depiction in **a** and the two-dimensional view in **b**, combining the 3-layer stacking sequence and the α, β alternation of neighbouring layers results in a 6-layer repeat sequence [Aα, Bβ, Cα, Aβ, Bα, Cβ] Aα,…, corresponding to a threefold repeat of the triclinic unit cell. Intralayer bonding between the NPs (α − α and β − β) occurs through twofold bundled ligands (L$_2$); see inter-NP regions along the vector **b** in **b**, and the connection between the NPs along the vector **a** in **d**, where a view of the (**a**,**c**) plane of the superlattice is given. The view in **d** illustrates also the interlayer hydrogen bonding between neighbouring NPs, involving triply bundled ligands (L$_3$). An enlargement of the hydrogen-bond region is given in inset (ii), showing two hydrogen bonds between each pair of interfacing ligands.

interfacing pairs of ligands (one ligand from each NP), with only a small contribution from interactions between the backbones of the ligands.

Insights into the nature of bonding and organization of NP-assembled superlattices may be obtained through investigations of their mechanical properties. Indeed, the mechanical response characteristics (that is bulk, Young and shear moduli, as well as

hardness and fracture toughness) of NPSLs, and their dependencies on composition, NP size, the capping ligands, and on the ambient conditions, are of fundamental interest[9], as well as of relevance for the design of NPSL-based devices. Measurements of the mechanical properties can be rather involved (requiring high-pressure measurements in conjunction with diffraction experiments, preferably using synchrotron radiation), and they are expected to show dependencies
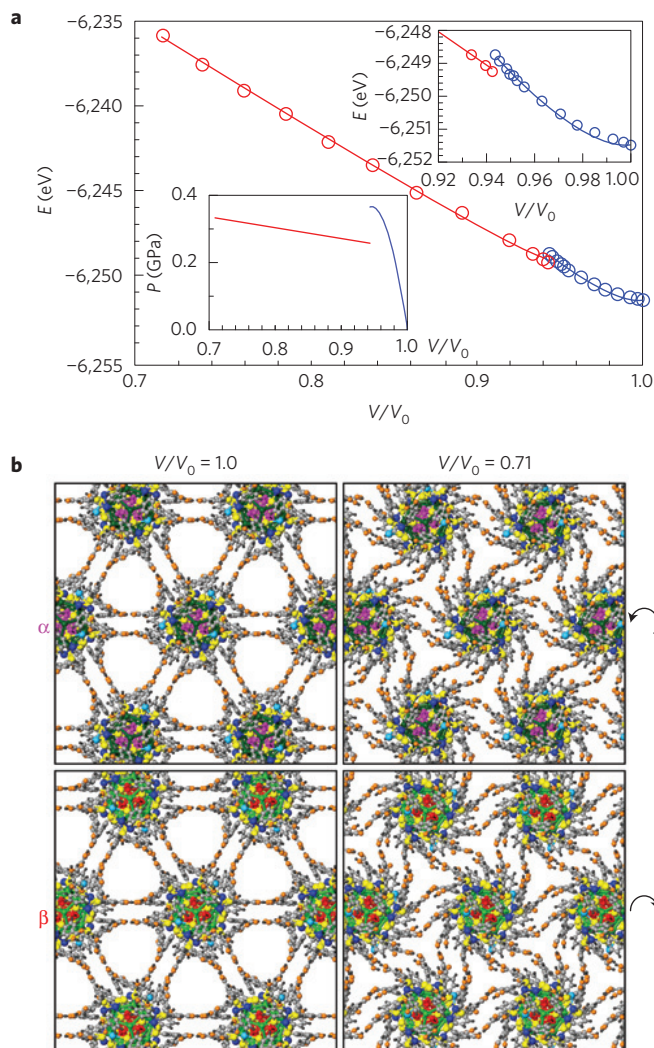
a, First-principles-calculated total energy of the superlattice plotted versus the compression parameter V/V_0, where $V \le V_0$ is the compressed volume of the unit cell and V_0 is the initial, equilibrium ($P = 0$) volume. The circles denote calculated values and the continuous lines give fits to the data: a third-order Birch expansion of the total energy $E(V)$ in the low-strain region (blue), and a second-order equation in the high-strain region (red). The transition between the two regions is at $C^* = 0.943$. The inset in the upper right gives an enlargement of the low-strain compression interval and the transition region. The inset at the bottom left depicts the pressure, obtained as the volume derivative of the best fit to the total energy in each of the compression regions, plotted versus V/V_0. **b**, Arrangement of the silver NPs in two neighbouring layers, viewed in the **ab** plane, with the NPs in the two layers (denoted as α and β) related by a mirror reflection in the $x = 0$ plane followed by a **c**/2 translation (see Fig. 1). The configurations on the left correspond to the $P = 0$ equilibrium state, (V/V_0) $= 1$, and the ones on the right were recorded at the end of the volume compression process ((V/V_0) $= 0.71$), showing reduced distance between the NPs' centres of mass, and exhibiting ligands' flexure and rotations of the NPs. All particles in the same layer (α or β) rotate in unison, but the NPs' rotations in the two layers are in opposite senses—anticlockwise in the α layer and clockwise in the β layer. For cluster rotations viewed in the **ac** plane, see Supplementary Information 5.

on the degree of order and dimensionality of the NPSL system. Consequently, relatively little is known so far (experimentally[18,19] and theoretically[9]) about the mechanical properties of NPSLs

compared with the significant progress made in explorations of their optical and electronic properties.

Figure 2a shows the first-principles calculated variation of the superlattice total energy in response to hydrostatic compression of the NPSL (Supplementary Information 2), expressed as $C = V/V_0$, where $V \le V_0$ is the compressed volume of the unit cell and V_0 is the initial equilibrium volume. In the simulations of the compression process, the initial configuration was taken as the triclinic unit cell of the NPSL (containing two $Na_4Ag_{44}(p\text{-MBA})_{30}$ NPs), optimized through relaxation of the X-ray-determined structure (for details of the compression simulations see Supplementary Information). Shown also (continuous lines) are fits obtained through use of the nth-order Birch[20] expansion of the total energy $E(V) = e_0 + e_1\varepsilon + e_2\varepsilon^2 + e_3\varepsilon^3 + \dots$ as a function of the Eulerian strain $\varepsilon = [(V/V_r)^{-2/3} - 1]/2$, where V_r is the reference volume; $V_r = V_0$ for the low-strain interval (shown in blue), where $n = 3$ in the expansion of $E(V)$, and $V_r = 23075.2$ Å^3 corresponds to the onset of the high-strain region (depicted in red), occurring for a compression $C \le C^* \equiv V/V_0 = 0.943$). The coefficients in the above expansion of the energy can be obtained (Supplementary Information 3) by using the relation for the pressure $P = -dE/dV$, and by relating changes in the energy to pressure-driven changes in the volume. In this way one finds that the fits to the energy variation in the low- and high-strain regions (see continuous lines in Fig. 2a) give as fitting coefficients the bulk modulus, $B_r = -[V dP/dV]_r$, and its pressure derivative $B_r' = [dB/dP]_r$, where the subscript r denotes the reference volume; for the fit in the low-strain region r $\equiv 0$, that is, $V_r = V_0$ (the volume of the system at zero pressure) and the fitting coefficients are denoted as B_0 and B_0', and in the high-strain region V_r is taken as the volume at the onset of that region. In the low-strain region we find $B_0 = 16.7$ GPa, and $B_0' = -17.5$. The calculated value of B_0 is in the range typical for molecular solids[21], and it is merely six times smaller than that of bulk silver[22] ($B_0 = 106.1$ GPa and $B_0' = 4.70$), indicating a rather rigid molecular framework where the collective mechanical response of the compositionally heterogeneous superlattice is determined largely by the compliance of the protecting organic ligands. The predicted negative value of B_0' is anomalous (most materials get stiffer for increasing applied pressure), indicating pressure-induced softening; we note that in archetypal hydrogen-bonded materials, that is, ice[23] (solidified water), $B_0' > 0$, whereas a large negative value, $B_0' = -8.6$ (with $B_0 = 36.9$ GPa), has been measured recently[24] for a molecular-framework material ($Zn(CN)_2$). In the high-strain compression interval we predict for the superlattice a greatly reduced bulk modulus $B_{HS} = 0.347$ GPa and $B_{HS}' = 0.37$, indicating that in the high-strain region the superlattice exhibits a typical soft-solid rheology.

The nature of the transition at C^* is revealed from examination of the arrangement of the silver NPs (see Fig. 2b, where two neighbouring layers, denoted on the left as the α and β layers, are shown). The configurations on the left correspond to the equilibrium state ($V/V_0 = 1$), exhibiting a closed-packed intralayer arrangement with each NP interacting through H bonds with six neighbouring NPs. The configurations on the right were recorded at the end of the volume compression process ($V/V_0 = 0.71$), where the NPs have come closer to each other. Most importantly, all NPs in a given layer rotated collectively in the same direction, but with the sense, or chirality, of the rotations in two neighbouring layers being opposite to each other; for images of the rotated NPs in neighbouring layers, see Supplementary Information 4. As we discuss below, the correlated rotations of the silver NPs are driven by compression-induced buckling of the ligands.

Examination of the variation of structural parameters (both intra- and inter-NP geometries) recorded during the simulated compression and shown in Fig. 3 (Supplementary Information 4 and 5) reveals the nature of the structural transition at C^*.
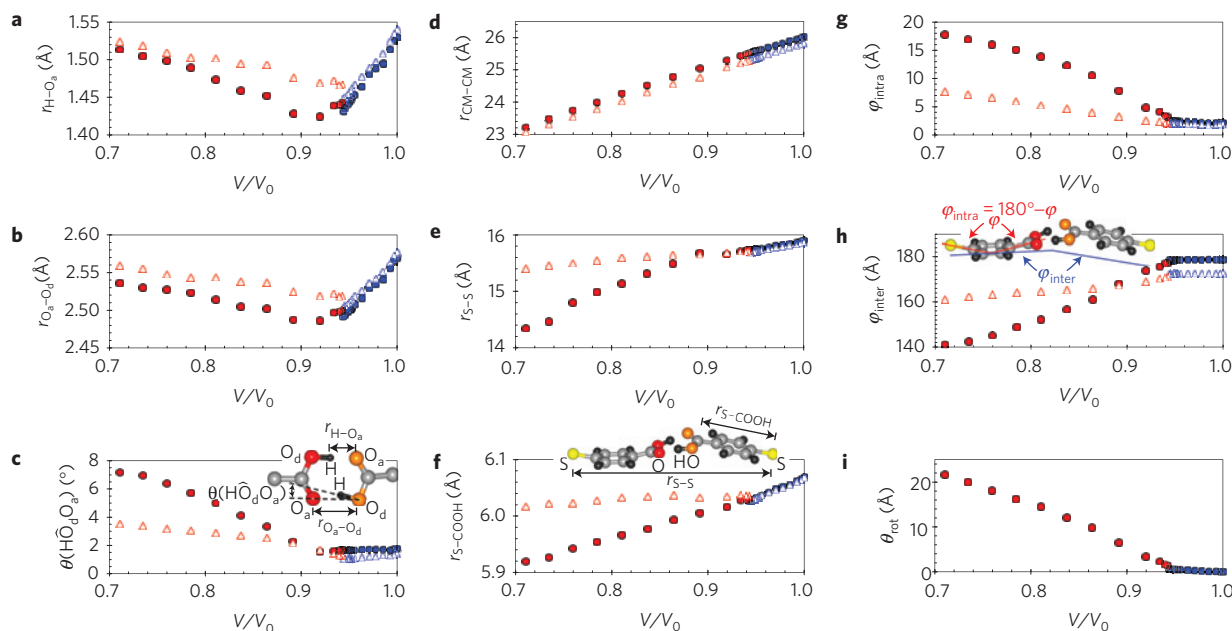
Figure 3 | Intra- and inter-NP distances and angles induced by the applied compression (V/V_0) of the superlattice. a–c, Hydrogen-bond parameters: r_{H-O_a}, distance between the bonding H atom and the acceptor oxygen (**a**); $r_{O_a-O_d}$, distance between the hydrogen-bonded acceptor and donor oxygen atoms (**b**); characteristic hydrogen-bond angle, $\theta(HO_dO_a)$ (**c**). **d–f,** Inter-NP distances: r_{CM-CM}, distance between the centres of mass (CM) of two neighbouring NPs (**d**); r_{S-S}, distance between the sulphur atoms of two hydrogen-bonded p-MBA ligands belonging to neighbouring silver NPs (**e**); r_{S-COOH}, distance between the S atom of a p-MBA ligand and the C atom of its carboxylic group (**f**). **g,h,** Buckling (flexure) and NP rotation angles: intraligand (**g**) and interligand (**h**) buckling angles induced by the volume compression. **i,** The rotation angle of the NPs (the rotations of the α and β NPs are chiral; that is, they rotate by the same amount but in opposite senses). The method for calculating θ_{rot} is given in Supplementary Information 7. Filled circles and open triangles correspond, respectively, to intralayer ($\alpha-\alpha$ and $\beta-\beta$) and interlayer ($\alpha-\beta$) distances, or angles. Blue and red correspond to the low- and high-strain intervals of the compression process. The various distances and angles are defined in the insets.

The structural information in Fig. 3 is organized as follows: hydrogen-bond region in Fig. 3a–c, p-MBA ligands' distances in Fig. 3d,e, and ligands' flexure angles and NPs' rotation in Fig. 3g–i; compression-induced variations in ligand torsion angles are given in Supplementary Information 5. To a good approximation the main structural modifications take place in the non-metal regions (see Fig. 3a–c,e–i and Supplementary Information 6), with the NPs' centres of mass getting closer together at a constant rate (Fig. 3d) during the compression (V/V_0). However, the onset of the high-strain compression stage is accompanied by a rotation of the NPs, with the metal cores revolving essentially as rigid bodies (Fig. 3i).

The physics underlying the correlated NPs' rotation is revealed by noting that for $V/V_0 \leq C^*$ the pattern of variation of parameters characterizing the ligands' conformations changes markedly; we also observe that the structural response to the compression is isotropic in the low-strain region ($V/V_0 > C^*$), acquiring an anisotropic character in the high-strain interval, with the intralayer variations being larger than the interlayer ones (compare circles and triangles, respectively). In particular, we note that the hydrogen-bond distance, and the characteristic angle, $\theta(HO_dO_a)$, increase in the high-strain compression interval. Following a methodology used in the analysis of bonding in water[25], we adapted a criterion stipulating that hydrogen bonding between the tails of interacting p-MBA ligands requires simultaneously that: $r_{O_a-O_d} < 2.85$ Å and $\theta(HO_dO_a) < 15°$. Employing this criterion we conclude that hydrogen bonding remains intact throughout the entire compression processes (Fig. 3a–c). We also observe that both the rate of decrease of the distance between the two sulphur atoms anchoring hydrogen-bonded p-MBA ligands to neighbouring NPs (r_{S-S}) and the intra- and inter-ligand flexure (φ_{intra}, φ_{inter}) grow in a marked manner past the transition. This implies that the rotational (chiral) response in the high-strain interval, driven by the buckling (flexure) of the ligands, originates from the inclination

to maintain the H bonds in place, acting as 'molecular hinges'. This results in the particular ligand-buckling pattern recorded in our first-principles simulations, with the consequent torque on the silver cores causing their correlated chiral rotations. These processes underlie the predicted compression-induced rheological transition of the NPSL from a rather 'stiff', pressure-softening molecular solid in the low-strain regime to a much softer material in the high-strain compression range.

The intricate structure of the superlattice made of Na$_4$Ag$_{44}$(p-MBA)$_{30}$ NPs that we have described and analysed here stands out as one of the more—perhaps, the most—complex molecular solids showing molecular-framework materials characteristics that have been synthesized, X-ray measured, and theoretically analysed so far. This superlattice is made of relatively large NPs (492 atoms) containing a metallic core (Ag$_{44}$) capped by organic ligands. These nanoscale building blocks were found to hold together by an elaborate hydrogen-bond network that is likely to have acted as a structure-directing 'synthon'[30], promoting the crystallization of the superlattice and endowing it with enhanced stability and unique properties. In particular, first-principles quantum-mechanical simulations predict pronounced pressure softening under hydrostatic compression, an anomalous behaviour found so far only for amorphous silica[31], ZrW$_2$O$_8$ (ref. 32) and Zn(CN)$_2$ (ref. 24). Furthermore, the emergent molecular-level mechanical response to the compressive stimulus was found to entail correlated chiral rotations of the NPs, like gears, or chiral honeycomb[34], with the flexured p-MBA ligands serving as torque-transfer relays and the hydrogen bonds acting as 'molecular hinges'.

With the growing interest in understanding the principles underlying the crystal engineering of materials with desired structure–function relationships, and in the development of materials with machine-like molecular-level responses to external stimuli,[33] the insights gained in this work may provide impetus

for future investigations into the molecular-scale design principles and unifying patterns that could guide future progress in these directions. Specifically, we foresee future explorations of the superlattice vibrational soft-mode dynamics underlying structural transitions in NPSLs, and investigations of the response of such superlattices to thermal stimuli. We expect that, in conjunction with the aforementioned pressure-induced softening anomaly, they would exhibit also negative thermal expansion.

Methods

Theoretical calculations employed the VASP-DFT (Vienna *ab initio* simulation package with density functional theory) package, a plane-wave basis with a kinetic energy cutoff of 400 eV, PAW (projector augmented wave) pseudopotentials[26] and the PW91 generalized exchange–correlation gradient approximation[27,28] (GGA). The number of atoms in these large-scale calculations (two Na_4Ag_{44}(*p*-MBA)$_{30}$ NPs in the NPSL triclinic unit cell) was 996 atoms with 4,036 valence electrons. The initial positions of the silver atoms and *p*-MBA ligands were taken from the X-ray-determined structure (the hydrogen atoms, as well as the four sodium atoms, were added to the structure and their positions were relaxed). We quote here results calculated for the centre of the Brillouin zone (Γ-point); we verified that inclusion of k-points does not have a noticeable effect on our results. Also, inclusion of van der Waals (vdW) interactions[29] between the ligands resulted in a relatively small increase in the cohesion of the NPSL. Thus, for the initial (uncompressed) X-ray-measured configuration of the superlattice, the total energies (with and without the vdW interaction) differ by $\delta E_{total} \equiv [E_{total}(DFT) - E_{total}(DFT+vdW)]/E_{total}(DFT+vdW)] = 0.525\%$, and the calculated cohesive energy is $E_{coh} = 0.91$ eV per *p*-MBA ligand, compared with 0.80 eV obtained without the vdW interactions; similar values are obtained for selected points along the compression process, for example at the last (first) point of the low (high)-strain compression intervals (Fig. 2a), the total energies, calculated with, and without, the vdW interaction, were found to differ by $\delta E_{total} = 0.545\%$ (0.54%), and at the end of the compression process ($V/V_0 = 0.71$) the calculated total energies differ by 0.6%. As a result of these findings and of uncertainties concerning the vdW corrections to DFT calculations, we quote results without vdW corrections. In optimizations of the structure of the periodic superlattice, performed initially as well as for each compression step, convergence was achieved for forces smaller than 0.002 eV Å^{-1}.

References

1. Brus, L. Electronic wave-functions in semiconductor clusters-experiment and theory. *J. Phys. Chem.* **90,** 2555–2560 (1986).
2. Murray, C. B., Kagan, C. R. & Bawendi, M. G. Self-organization of CdSe nanocrystals into three-dimensional quantum dot superlattices. *Science* **270,** 1336–1338 (1995).
3. Whetten, R. L. *et al.* Nanocrystal gold molecules. *Adv. Mater.* **8,** 428–433 (1996).
4. Luedtke, W. D. & Landman, U. Structure, dynamics, and thermodynamics of passivated gold nanocrystallites and their assemblies. *J. Phys. Chem.* **100,** 13323–13329 (1996).
5. Bruchez, J. M., Moronne, M., Gin, P., Weiss, S. & Alivisatos, A. P. Semiconductor nanocrystals as fluorescent biological labels. *Science* **281,** 2013–2016 (1998).
6. Whetten, R. L. *et al.* Crystal structures of molecular gold nanocrystal arrays. *Acc. Chem. Res.* **32,** 397–406 (1999).
7. Link, S. & El-Sayed, M. A. Spectral properties and relaxation dynamics of surface plasmon electronic oscillations in gold and silver nanodots and nanorods. *J. Phys. Chem. B* **40,** 8410–8426 (1999).
8. Maier, S. A. *et al.* Plasmonics - A route to nanoscale optical devices. *Adv. Mater* **13,** 1501–1505 (2001).
9. Landman, U. & Luedtke, W.D. Small is different: Energetic, structural, thermal and mechanical properties of passivated nanocluster assemblies. *Faraday Discuss.* **125,** 1–22 (2004).
10. Anker, J. N. *et al.* Biosensing with plasmonic nanosensors. *Nature Mater.* **7,** 442–453 (2008).
11. Atwater, H. A. & Polman, A. Plasmonics for improved photovoltaic devices. *Nature Mater.* **9,** 205–213 (2010).
12. Talapin, D. V., Lee, J-S., Kovalenko, M. V. & Shevchenko, E. V. Prospects of colloidal nanocrystals for electronic and optoelectronic applications. *Chem. Rev.* **110,** 389–458 (2010).
13. Goodfellow, B. W. & Korgel, B. A. Reversible solvent vapor-mediated phase changes in nanocrystal superlattices. *ACS Nano* **5,** 2419–2424 (2011).
14. Hanrath, T. Colloidal nanocrystal quantum dot assemblies as artificial solids. *J. Vac. Sci. Technol. A* **30,** 030802 (2012).
15. Arvizo, R. R. *et al.* Intrinsic therapeutic applications of noble metal nanoparticles: Past, present and future. *Chem. Soc. Rev.* **41,** 2943–2970 (2012).
16. Desireddy, A. *et al.* Ultrastable silver nanoparticles. *Nature* **501,** 399–402 (2013).
17. Anderson, P. W. More is different. *Science* **177,** 393–396 (1972).
18. Mueggenburg, K. E., Lin, X-M., Goldsmith, R. H. & Jaeger, H. M Elastic membranes of close-packed nanoparticle arrays. *Nature Mater.* **6,** 656–660 (2007).
19. Podsiadlo, P. *et al.* The role of order, nanocrystal size, and capping ligands in the collective mechanical response of three-dimensional nanocrystal solids. *J. Am. Chem. Soc.* **132,** 8953–8960 (2010).
20. Birch, F. Finite strain isotherm and velocities for single-crystal and polycrystalline NaCl at high pressures and 300° K. *J. Geophys. Res.* **83,** 1257–1268 (1978).
21. Orgzall, I., Emmerling, F., Burkhard, S. B. & Franco, O. High-pressure studies on molecular crystals—relations between structure and high-pressure behavior. *J. Phys. Condens. Matter* **2,** 1–15 (2008).
22. Syassena, K. & Holzapfel, W. B. Isothermal compression of AI and Ag to 120 kbar. *J. Appl. Phys.* **49,** 4427–4430 (1978).
23. Yoshimura, Y., Stewart, S. T., Somayazulu, M., Mao, H-K. & Hemley, R. J. High-pressure X-ray diffraction and Raman spectroscopy of ice VIII. *J. Chem. Phys.* **124,** 024502 (2006).
24. Collings, I. E. *et al.* Homologous critical behavior in the molecular frameworks Zn(CN)$_2$ and Cd(imidazolate)$_2$. *J. Am. Chem. Soc.* **135,** 7610–7620 (2013).
25. Luzar, A. & Chandler, D. Hydrogen-bond kinetics in liquid water. *Nature* **379,** 55–57 (1996).
26. Kresse, G. & Joubert, D. From ultrasoft pseudopotentials to the projector augmented-wave method. *Phys. Rev. B* **59,** 1758–1775 (1999).
27. Perdew, J. P. in *Electronic Structure of Solids '91* (eds Ziesche, P. & Eschrig, H.) 11–20 (Akademie Verlag, 1991).
28. Perdew, J. P. *et al.* Atoms, molecules, solids, and surfaces: Applications of the generalized gradient approximation for exchange and correlation. *Phys. Rev. B* **46,** 6671–6687 (1992) ; *Erratum* **48,** 4978–4978 (1993).
29. Grimme, S. Semiempirical GGA-type density functional constructed with a long-range dispersion correction. *J. Comput. Chem.* **27,** 1787–1799 (2006).
30. Desiraju, G. R. Supramolecular synthons in crystal engineering—a new organic synthesis. *Angew. Chem. Int. Ed.* **34,** 2311–2327 (1995).
31. Tsiok, O. B., Brazhkin, V. V., Lyapin, A. G. & Khvostantsev, L. G. Logarithmic kinetics of the amorphous-amorphous transformations in SiO$_2$ and GeO$_2$ glasses under high-pressure. *Phys. Rev. Lett.* **80,** 999–1002 (1998).
32. Pantea, C. *et al.* Pressure-induced elastic softening of monocrystalline zirconium tungstate at 300 K. *Phys. Rev. B* **73,** 214118 (2006).
33. Khuong, T-A. V., Nuez, J. E., Godinez, C. E. & Garcia-Garibay, M. A. Crystalline molecular machines: A quest toward solid-state dynamics and function. *Acc. Chem. Res.* **39,** 413–422 (2006).
34. Lakes, R. Deformation mechanisms in negative Poisson's ratio materials: Structural aspects. *J. Mater. Sci.* **26,** 2287–2292 (1991).

Author contributions

U.L. conceived and directed the theoretical work, analysed the experimental and theoretical results, and wrote the manuscript. B.Y. performed the DFT computations. B.Y., W.D.L., R.N.B. and J.G. participated in the analysis of the computational and experimental results. T.P.B. conceived, directed and analysed the experimental research, and A.D. and B.E.C. performed the experimental work. All authors contributed to preparation of the final manuscript.

Additional information

Supplementary information is available in the online version of the paper. Reprints and permissions information is available online at www.nature.com/reprints. Correspondence and requests for materials should be addressed to U.L.

Competing financial interests

The authors declare no competing financial interests.

Hydrogen-bonded structure and mechanical chiral response of a silver nanoparticle superlattice

Bokwon Yoon, W. D. Luedtke, Robert N. Barnett, Jianping Gao, Anil Desireddy, Brian E. Conn, Terry Bigioni and Uzi Landman

In the version of this Letter originally published online, in Fig. 1a, the yellow arrow was duplicated. This error has now been corrected in all versions of the Letter.